Model Simulations of a Shock-Cloud Interaction in the Cygnus Loop

Daniel J. Patnaude
Dartmouth College

Robert A. Fesen
Dartmouth College

MODEL SIMULATIONS OF A SHOCK-CLOUD INTERACTION IN THE CYGNUS LOOP

Daniel J. Patnaude[1,2] and Robert A. Fesen[1]

ABSTRACT

We present optical observations and two-dimensional hydrodynamic modeling of an isolated shocked ISM cloud. Hα images taken in 1992.6 and 2003.7 of a small optical emission cloud along the southwestern limb of the Cygnus Loop were used to measure positional displacements of $\sim 0\rlap{.}''1$ yr^{-1} for surrounding Balmer-dominated emission filaments and $0\rlap{.}''025$–$0\rlap{.}''055$ yr^{-1} for internal cloud emission features. These measurements imply transverse velocities of $\simeq 250$ and $\simeq 80$–140 km s^{-1} for ambient ISM and internal cloud shocks, respectively. A lack of observed turbulent gas stripping at the cloud-ISM boundary in the Hα images suggests that there is not an abrupt density change at the cloud-ISM boundary. Also, the complex shock structure visible within the cloud indicates that the cloud's internal density distribution is two-phased—a smoothly varying background density that is populated by higher density clumps. Guided by the Hα images, we present model results for a shock interacting with a nonuniform ISM cloud. We find that this cloud can be well modeled by a smoothly varying power-law core with a density contrast of ~ 4 times the ambient density, surrounded by a low-density envelope with a Lorentzian profile. The lack of sharp density gradients in such a model inhibits the growth of Kelvin-Helmholtz instabilities, consistent with the cloud's appearance. Our model results also suggest that cloud clumps have densities ~ 10 times the ambient ISM density and account for $\sim 30\%$ of the total cloud volume. Moreover, the observed spacing of internal cloud shocks and model simulations indicate that the distance between clumps is ~ 4 clump radii. We conclude that this diffuse ISM cloud is best modeled by a smoothly varying, low-density distribution coupled to higher density, moderately spaced internal clumps.

Subject headings: hydrodynamics — ISM: individual (Cygnus Loop) — ISM: kinematics and dynamics — shock waves — supernova remnants

1. INTRODUCTION

The interaction of shock waves with the interstellar medium (ISM) such as those associated with supernovae (SNe), stellar winds, bipolar flows, H II regions, or spiral density waves is a fundamental process in interstellar gas dynamics and is key to understanding the evolution and structure of the ISM. The highly nonlinear interaction between SN-generated shocks and interstellar clouds is often not suited to analytic approaches but requires a multidimensional hydrodynamics study of the shock-cloud problem using high-resolution methods.

A hydrodynamical study of a shocked ISM cloud was made by Klein et al. (1994, hereafter KMC94), who found that the cloud may be destroyed by a series of instabilities associated with the postshock flow of intercloud gas past the cloud. Earlier work on this problem includes that of Woodward (1976) and Nittmann et al. (1982). More recently, Poludnenko et al. (2002) studied the role that internal cloud structure plays in the destruction of the cloud.

For investigating shocked ISM cloud physics, the interaction between a SN shock and low-density diffuse ISM clouds is of particular interest. Supernova remnants (SNRs) shape and enrich the chemical and dynamical structure of the ISM, which, in turn, affects the evolution of subsequent SNRs. The details of just how SN-generated shock waves interact with interstellar clouds are not well understood.

There are several limiting factors in attempting to compare model simulations to observed SNR shock-cloud interactions.

While models can be viewed edge-on and rotated in two or three dimensions, shocked interstellar clouds are viewed only in projection, which leads to a complex-looking shock structure due to multiple and overlapping shocks. In addition, one observes only a single epoch, i.e., a "snapshot," of the interaction. These factors make it difficult to understand and model the time-dependent kinematics and detailed dynamical processes of the interaction. Also, contrary to how they are often modeled, real interstellar clouds are neither cylindrical or spherical in shape nor sharp-edged, with interiors very likely nonuniform in density. Furthermore, many shocked interstellar clouds are dense enough that radiative losses, which can alter the overall dynamics of the shock-cloud interaction, are important (Mellema et al. 2002; Fragile et al. 2004). Finally, the inclusion of an embedded magnetic field can drastically alter the dynamics of the interaction. For instance, a strong, ordered magnetic field can suppress dynamical instability growth predicted by fluid dynamical simulations (Mac Low et al. 1994; Fragile et al. 2005).

In looking for an "ideal" shock-cloud interaction, one would like to avoid many of the aforementioned effects, and the Cygnus Loop SNR affords several distinct advantages. Because of the remnant's large angular size ($2\rlap{.}°8 \times 3\rlap{.}°5$), low foreground extinction [$E(B-V) = 0.08$ mag; Parker 1967; Fesen et al. 1982], and wide range of shock conditions, the Cygnus Loop is one of the better locations for studying the ISM shock physics of middle-aged remnants. At a distance of 550^{+110}_{-80} pc (Blair et al. 2005), it has a physical size of 27 pc $\times$ 33.5 pc. Located $8\rlap{.}°5$ below the galactic plane, the remnant lies in a multiphase medium containing large ISM clouds with a hydrogen density of $n = 5$–10 cm^{-3}, surrounded by a lower density intercloud component of $n \approx 0.1$–0.2 cm^{-3} (DeNoyer 1975).

Recently, Patnaude et al. (2002) studied a small, isolated cloud along the southwest limb of the Cygnus Loop that met

[1] Physics and Astronomy Department, Dartmouth College, 6127 Wilder Laboratory, Hanover, NH 03755.
[2] Smithsonian Astrophysical Observatory, 60 Garden Street, Cambridge, MA 02138.

many of the desired cloud properties for investigating shock-cloud interactions. This cloud is relatively small (∼2′ in radius; 0.32 pc at 550 pc; Blair et al. 2005), exhibits a fairly uncomplicated, line-of-sight internal structure and lies isolated from other shocked ISM clouds. Moreover, the shock-cloud interaction is dominated by nonradiative, or "Balmer-dominated" filaments, indicating that the cloud-shock dynamics is not significantly affected by postshock radiative losses.

Here we present a new analysis of this small shocked cloud. Proper motion measurements and inferred shock velocities of individual filaments in and surrounding the cloud are presented. These results were used to estimate the initial conditions for hydrodynamical model simulations of a shock interaction with an unmagnetized, lumpy cloud. In § 2 these new observations are presented, as well as the technique used to measure the filament proper motions. Model parameter estimates are then discussed in § 3. Our hydrodynamical models are presented in § 4, where proper motion and density estimates are implemented in the model initial conditions. Model results are presented in § 5 and compared to the southwest cloud in § 6; our conclusions are given in § 7.

2. OBSERVATIONS

Narrowband Hα images of the southwest region of the Cygnus Loop were obtained on 1992 July 7 and 2003 August 29 using the MDM 2.4 m Hiltner telescope. For the 1992 July images, four 600 s Hα filter (FWHM = 80 Å) exposures were acquired with a Loral 2048×2048 front-side–illuminated CCD yielding a spatial resolution of 0″.343 pixel⁻¹. Details of the 1992 observations and subsequent data reduction can be found in Patnaude et al. (2002).

Two 1000 s Hα filter (FWHM = 15 Å) exposures were taken in 2003 August with a SITe 2048×2048 back-side–illuminated CCD with a resolution of 0″.275 pixel⁻¹. Using the Image Reduction and Analysis Facility (IRAF),[3] the data were bias-subtracted and flat-fielded, and cosmic-ray hits were removed. The resulting 2003 epoch image is shown in Figure 1. Globally, the cloud's morphology is nearly identical to that seen in the 1992 images (Patnaude et al. 2002, Figs. 2 and 3), but close inspection between the two epoch images showed measurable proper motions for both internal cloud structures and the surrounding thin shock front filaments.

3. ANALYSIS AND RESULTS

Following the procedure described by Thorstensen et al. (2001), the coordinate systems of the two Hα images were aligned using DAOPHOT in conjunction with the USNO-A2.0 catalog. The data sets were then rebinned to an effective image scale of 0″.1 pixel⁻¹. This rebinning introduced a small global offset of −0″.07 pixel⁻¹ between the two images, uniform across the entire field of view.

3.1. Proper Motion Measurements

Individual filament regions for the proper motion analysis were selected based on their projection onto the plane of the sky, the complexity of the filament and surrounding regions, and the brightness of the filament feature. Based on these criteria, 14 filaments within the cloud, including both Balmer-dominated and
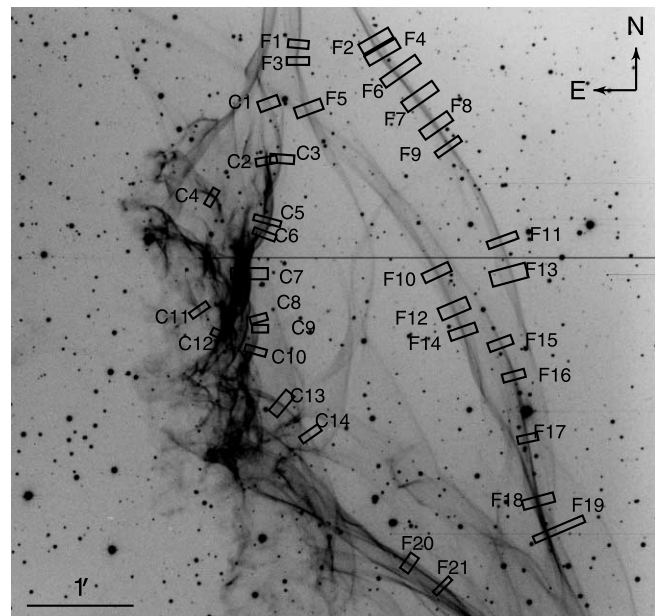
Fig. 1.—2003 August MDM 2.4 m Hα image of the southwest cloud in the Cygnus Loop showing the locations of our selected filaments.

radiative filaments, and 21 regions from the surrounding Balmer-dominated shock front were chosen (see Fig. 1).

One-dimensional intensity profiles were extracted for each region, and the pixel shift in each shock filament was computed using the IRAF task xcsao, which is based on the software of Tonry & Davis (1979). While this task was written to compute relative radial velocities via the cross-correlation function between two spectra, the cross-correlation function yields accurate filament motions in terms of pixel shifts between two images. For thin Balmer-dominated filaments and bright and sharp cloud-shock features, the cross-correlation analysis was able to match the shock fronts between the two epochs and measure the pixel shift between the two data sets to an accuracy of 10%–15%. The results from this analysis are listed in terms of proper motion (mas yr⁻¹) and transverse velocity (km s⁻¹) in Table 1. The quoted velocities assume a distance of 550^{+110}_{-80} pc (Blair et al. 2005).

Example data and cross-correlation functions for two regions are shown in Figure 2. These one-dimensional filaments and cross-correlation functions are representative of the data for the nonradiative filaments (Fig. 2, *left*) and internal cloud filaments (Fig. 2, *right*), where there is often a plateau of emission (from shocked cloud material) downstream from the shock front and then a steep rise in emission at the cloud-shock front.

Quoted errors in Table 1 include the signal-to-noise ratio (S/N) in the filament region, the curvature of the filament region, the profile of the filament when convolved with the image point-spread function (FWHM₁₉₉₂ = 1″.0; FWHM₂₀₀₃ = 0″.7), and the contribution from the background, local nebulosity, and adjacent filaments. For well-resolved filaments, the cumulative effect of these errors is ∼0.6 pixels, or about 10 km s⁻¹.

3.2. Estimate of Cloud Parameters

As discussed in Patnaude et al. (2002), this shock-cloud interaction is nearly tangent along the line of sight to the southwestern limb of the southern region of the Cygnus Loop. The cloud is being run over by the remnant's shock front, which is moving roughly east-west. We have divided the cloud into two regions: the ISM shock front and the cloud-shock region. Using the filament

TABLE 1
MEASURED PROPER MOTIONS AND ESTIMATED SHOCK VELOCITIES

Filament Region	$\Delta_r{}^a$ (mas)	μ (mas yr^{-1})	$V_s{}^b$ (km s^{-1})
Nonradiative Filaments			
F1	630 ± 55	55 ± 5	140 ± 10
F2	610 ± 55	55 ± 4	140 ± 10
F3	745 ± 55	65 ± 3	170 ± 10
F4	665 ± 55	60 ± 3	155 ± 10
F5	810 ± 55	70 ± 5	180 ± 10
F6	910 ± 80	80 ± 7	210 ± 15
F7	1075 ± 110	95 ± 9	250 ± 20
F8	960 ± 80	85 ± 6	220 ± 15
F9	780 ± 55	70 ± 2	180 ± 10
F10	1025 ± 55	90 ± 7	235 ± 10
F11	1010 ± 110	90 ± 10	235 ± 20
F12	900 ± 140	80 ± 12	210 ± 25
F13	1110 ± 55	100 ± 4	260 ± 10
F14	1120 ± 85	100 ± 6	260 ± 15
F15	745 ± 55	65 ± 4	170 ± 10
F16	625 ± 55	55 ± 4	145 ± 10
F17	800 ± 55	70 ± 3	185 ± 10
F18	715 ± 55	60 ± 2	155 ± 10
F19	690 ± 55	60 ± 4	155 ± 10
F20	720 ± 110	60 ± 9	155 ± 20
F21	660 ± 55	60 ± 4	155 ± 10
Cloud Filaments			
C1	620 ± 170	55 ± 15	140 ± 30
C2	325 ± 55	30 ± 3	80 ± 10
C3	575 ± 55	50 ± 4	130 ± 10
C4	410 ± 55	35 ± 2	90 ± 10
C5	400 ± 55	35 ± 5	90 ± 10
C6	500 ± 55	45 ± 5	120 ± 10
C7	340 ± 85	30 ± 6	80 ± 15
C8	550 ± 85	50 ± 7	130 ± 15
C9	380 ± 160	35 ± 13	90 ± 30
C10	425 ± 130	40 ± 11	105 ± 25
C11	280 ± 85	25 ± 8	65 ± 15
C12	295 ± 55	25 ± 2	65 ± 10
C13	380 ± 55	35 ± 4	90 ± 10
C14	410 ± 110	40 ± 10	105 ± 20

a 1992.6–2003.7
b Shock velocities assume a distance of 550 pc (Blair et al. 2005).

velocities listed in Table 1, we estimated an interstellar shock velocity of 250 km s^{-1} associated with the Balmer-dominated filaments. The wide range of Balmer filament velocities observed (140–260 km s^{-1}) may be due in part to density fluctuations around the cloud and the fact that only one component of the filament velocity is measured. That is, for filaments that are highly curved, the space velocity of the shock might be 200 km s^{-1}, but the local *measured* velocity might be in a direction other than perpendicular to our line of sight. Furthermore, although filaments were chosen based on selective criteria, factors such as low S/N, as well as adjacent, overlapping filaments contributed in some cases to a poorer cross-correlation between the two images. Nonetheless, our estimated shock velocity ≃250 km s^{-1} is consistent with the X-ray shock velocity of ∼300 km s^{-1} inferred from the *Röntgensatellit* (*ROSAT*) PSPC measurements (Patnaude et al. 2002).

The shocked cloud can be further divided into regions where the cloud shock is interacting with the cloud and where it is interacting with cloud clumps or "cloudlets." In general, the inferred shock velocities vary widely (65–140 km s^{-1}). This suggests that the density structure of the cloud is fairly complex, as the cloud shock appears to have been slowed less in certain areas relative to others.

Using these measurements, we adopt a shock velocity range inside the cloud of 60–100 km s^{-1}. These estimated cloud-shock velocities in turn imply a range of density contrasts in the cloud. Assuming ram pressure equilibrium ($\rho_a v_s^2 \approx \rho_c v_{cs}^2$), the density contrast between the cloud and the ambient medium, $\chi \equiv \rho_c/\rho_a$, is ∼4–17, with higher values representing areas populated with cloudlets and lower values representing regions of low density within the cloud.

The low-density nature of this cloud permits us to view its internal shock dynamics. We have used the structure and spacing of the internal shock fronts to estimate the clumpiness of the cloud. The easiest place to do this is at the western nose of the cloud (regions C8–C10). Measurements suggest that the postshock spacing of clumps in the cloud is ∼10″–30″. The upper limits correspond to shocks that are more highly evolved, while the lower limit corresponds to "small" shocks. Based on the size of the cloud (2′–4′ diameter), the cloudlets likely account for 30% of the total cloud volume. Furthermore, using a maximum compression of ∼4 for cloud clumps, we estimate the spacing between cloudlets to be ≈4–5 cloudlet radii (a_{cloudlet}).

4. HYDRODYNAMICAL MODELS

For modeling this shock-cloud interaction, we have used the numerical hydrodynamics software VH-1 (Blondin & Knerr 1992; Stevens et al. 1992), which implements the piecewise parabolic method (PPM) to solve the equations of gas dynamics (Colella & Woodward 1984). The PPM approach incorporates a fixed computational grid to evolve the standard conservation equations of mass, momentum, and energy. We assume an ideal, inviscid fluid with a ratio of specific heats, γ, equal to 5/3. VH-1 does not explicitly treat the collisionless shock physics associated with Balmer-dominated shocks. However, the goal of this study is to understand how a blast wave interacts with a diffuse ISM cloud. For these purposes, VH-1 serves as an excellent tool for tracing the motion and dynamics of this interaction.

Simulations were performed on a 1440×1440 Cartesian grid. The fiducial physical size of the square grid is 1×1, with $dx = dy = 6.9 \times 10^{-4}$. The size of the cloud sets the scale of the models. The cloud is ≈2′ in radius (≈10^{18} cm × $d_{550\,\text{pc}}$). On average, the cloud radius is 30% of the computational grid, or ≈450 cells per cloud radius. Therefore, the physical length scale of the grid $\Delta x \approx 2 \times 10^{15}$ cm cell^{-1}.

We estimate the importance of radiative losses by calculating the cooling timescale and comparing it to dynamically relevant timescales (mainly, the cloud crushing time and the pressure variation timescale). In general, radiative losses will be considered important if the cooling time is comparable to or shorter than the cloud-crushing time. We estimate the cooling time using the approximation of Kahn (1976), $t_{\text{cool}} = Cv^3/\rho$, where v is the cloud-shock velocity in units of km s^{-1}, ρ is the cloud density in units of gm cm^{-3}, and C is a constant = 6.0×10^{-35}. Assuming a cloud-shock velocity of 140 km s^{-1} and a cloud density of 10^{-24} gm cm^{-3}, we estimate a cooling time $t_{\text{cool}} > 5000$ yr. In contrast, the cloud-crushing time, $t_{\text{cc}} \equiv \chi^{1/2} a_0/v_b$, is ≈3800 yr, for a blast wave velocity of 250 km s^{-1} and an initial cloud radius of $a_0 = 0.3$ pc. Furthermore, the pressure variation timescale is ∼$0.1 t_{\text{cc}}$ (KMC94), which is <t_{cool}. Thus, it appears that neglecting the effects of cooling in our models will not have a significant impact on our results. This is supported by Patnaude et al. (2002), who showed that this cloud is only weakly radiative.
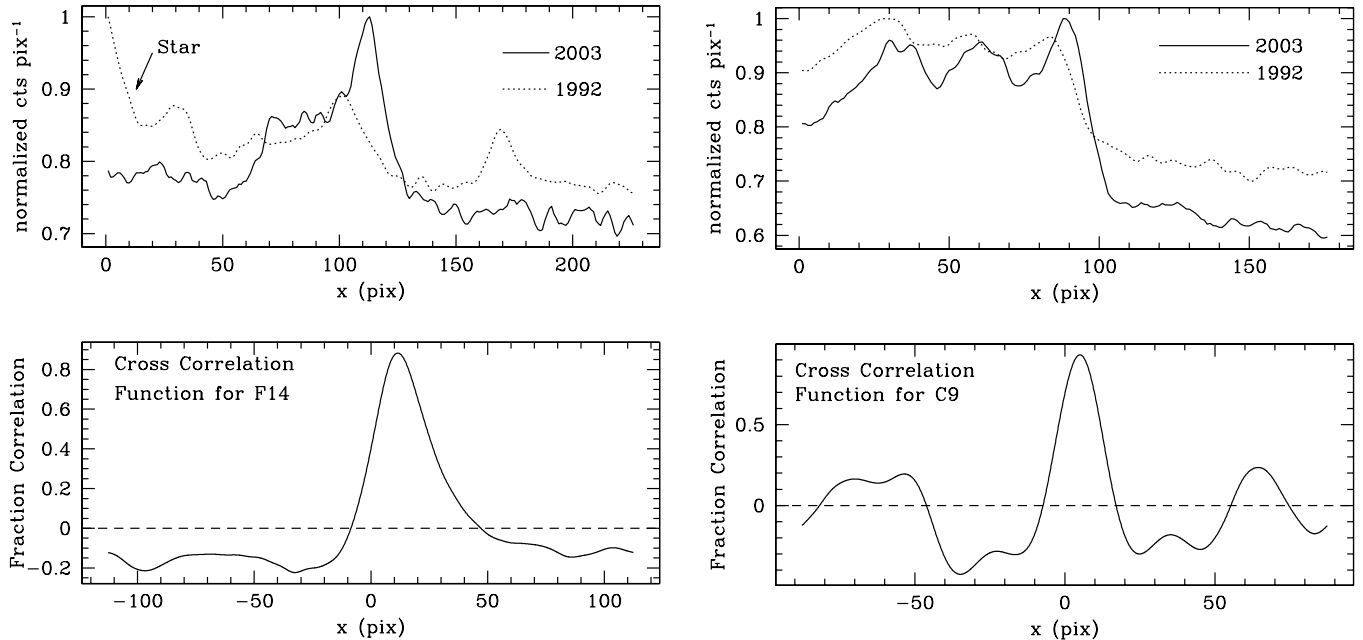
Fig. 2.—*Left*: One-dimensional shock profiles (*top*) and cross-correlation function (*bottom*) for region F14. The star appearing in the 1992 data (*top left*) is the result of using a wider filter during the 1992 observations. *Right*: Cloud-shock profile (*top*) and cross-correlation function (*bottom*) for region C9.

Under the assumptions that radiative losses are not dynamically important and that magnetic fields are not present (or that the cloud is only weakly magnetized), the shock-cloud interaction can be wholly defined by two parameters (KMC94), the shock Mach number, and χ, the density contrast of the cloud. Assuming an ISM sound speed of ≈ 10–15 km s^{-1} and a blast wave velocity of 250 km s^{-1}, we estimate a shock Mach number of $M \approx 20$. Furthermore, as pointed out in § 3, we estimate a cloud to ISM density contrast of $\chi \approx 6$.

To further simplify the problem, we chose a set of nondimensional variables such that the ISM density ρ_a is set to the ratio of specific heats, $\gamma = 5/3$, and the ISM pressure, P_a, is set to unity. The ISM sound speed, c_a, is thus set to 1 [$c_a = (\gamma P_a / \rho_a)^{1/2}$], and the shock velocity v_b is just the shock Mach number.

Model results by KMC94 suggested that a cloud radius should be at least on the order of 120 cells. For our models here, we chose the main cloud to have a radius of 300–500 cells ($\simeq 10^{17}$–10^{18} cm). The internal cloudlets have sizes that are 10%–20% of the cloud radius. Therefore, the cloudlets are only 33% of the suggested size. This small cloudlet size limits our ability to resolve instability growth along their boundaries. However, the goal here is to understand the global, internal morphology of the cloud, rather than the small-scale mixing within the cloud.

We broke the cloud's density structure into two parts: a background density profile and a clumping or density perturbation distribution. The background density distribution is chiefly responsible for the large-scale shock features, such as how the shock drapes over the cloud edges, while also defining the initial internal cloud-shock velocity. In contrast, the internal cloud density perturbations lead to the formation of small-scale shock structures within the cloud and have little effect on the cloud–ambient medium boundary layer.

On the basis of the cloud's emission features (Fig. 1), we assume that the large-scale density structure of the cloud is smoothly varying. The interface between the blast wave and the cloud shock, seen along the northern and southern periphery of the cloud, appears smooth. This suggests that the cloud is surrounded by a low-density envelope. There is no evidence to suggest that the central

density is sharply peaked, so we assume that at some inner radius the density profile turns over and becomes relatively constant throughout. Therefore, we assume that the cloud consists of a smoothly varying core surrounded by a low-density envelope. A function that fits this description is a truncated Lorentzian coupled to a power-law core:

$$\chi(r) = \begin{cases} \dfrac{\chi_{\max}}{1 + r_i^2/r_0^2}\left[1 + \Delta\left(\dfrac{r_i - r}{r_i}\right)^{\alpha}\right] & 0 \le r \le r_i, \\[3mm] \dfrac{\chi_{\max}}{1 + r^2/r_0^2} & r_i < r \le a_0, \end{cases} \tag{1}$$

where $r_0^2 = a_0^2/(\chi_{\max} - 1)$, $\Delta = 0.11$ sets the maximum core density, and α is the power-law index $= 0.5$, which ensures continuity across the core-envelope interface.

While the fine-scale structure of density perturbations within the cloud is not known, the lack of observed dynamical instabilities (at the resolution of the observations) suggests that such perturbations are probably smoothly varying. Therefore, for models using the above cloud density distribution, we chose to model the cloudlets as Gaussians. The spacing of the Gaussians is such that $\Delta r \approx 4\,\sigma$ between the cloudlet cores, which is consistent

TABLE 2
MODEL PARAMETERS

Model	a_0	$\chi_{\max}$	M	n_{cloudlet}	χ_{cloudlet}	a_{cloudlet}
1..................	0.30	6	20	...	...	...
2..................	0.25	10	10	...	...	...
3..................	0.30	6	20	13	10	0.03
4..................	0.30	3	20	13	10	0.03
5..................	0.35	10	10	15	10	0.05
6..................	0.35	8	10	15	15	0.03

NOTE.—Models 1, 3, and 4 have cylindrical density distributions. Models 2, 5, and 6 have distributions corresponding to eq. (1).
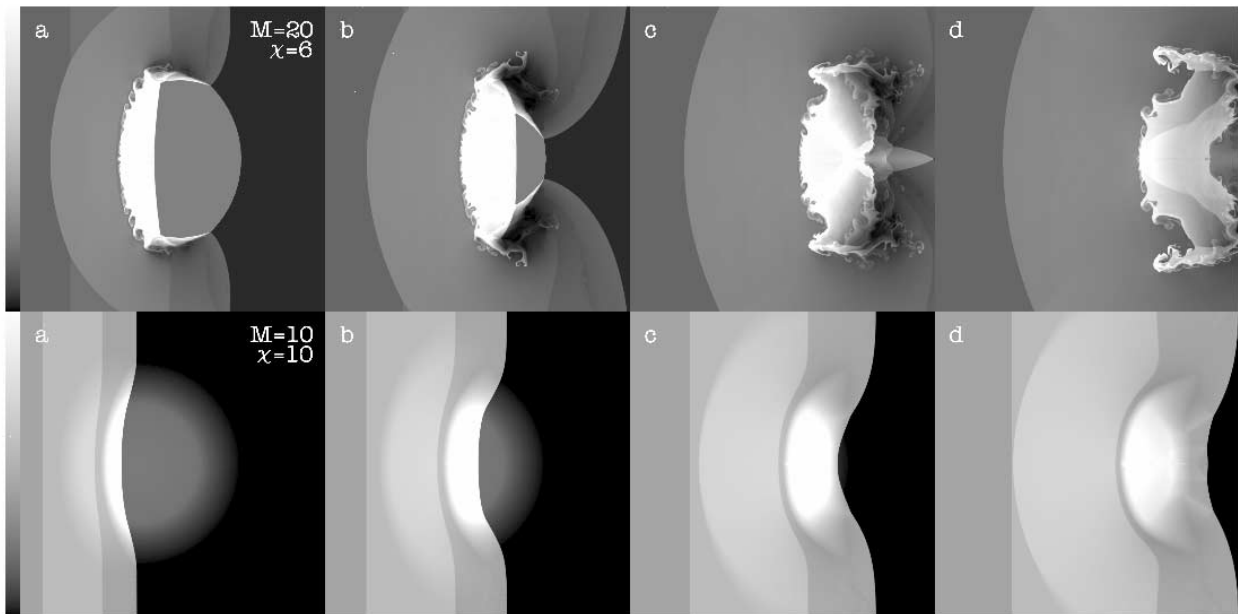
Fig. 3.—Density plots of models 1 (*top*) and 2 (*bottom*). Model 1 is shown at $t = (1.4, 2.6, 3.6, \text{and } 4.6) \times 10^{-2}$. Model 2 is shown at $t = (3.7, 5.5, 6.9, \text{and } 8.2) \times 10^{-2}$.

with the optimal spacing of $\Delta r \approx 4.2 a_{\text{cloudlet}}$ suggested by Poludnenko et al. (2002). Individual model parameters are listed in Table 2. For comparison, we include models of cylindrical clouds with similar density distributions.

5. RESULTS

Our basic shock-cloud interaction, model 1, is shown in the top panels of Figure 3. This model is of a Mach 20 shock interacting with a cloud of radius $a_0 = 0.3$ and constant density contrast $\chi = 6$. Figure 3 shows the model at $t = (1.4, 2.6, 3.6, \text{and } 4.7) \times 10^{-2}$. Figure 3c ($t = 3.6 \times 10^{-2}$) shows the model at approximately one cloud-crushing time (the cloud-crushing time, given by eq. [2.3] of KMC94, is $t_{\text{cc}} \approx 3.7 \times 10^{-2}$). According to KMC94, the growth time for Kelvin-Helmholtz (K-H) instabilities is $t_{\text{KH}} \approx \chi^{1/2}/(k v_{\text{rel}})$, where v_{rel} is the relative ve-

locity between the shocked cloud and the shocked ambient medium.

The relative velocity between the post–cloud-shock material and the postshock ambient material is given to first order by the relative jump conditions between the cloud and the ambient medium. Since $M \propto \chi^{1/2}$, $t_{\text{KH}} \sim \chi^{1/2} t_{\text{cc}}$ (for $k \sim a_0$). Higher wavenumber perturbations will form on a shorter timescale. In Figure 3c, there is clear evidence for K-H growth along the back side of the cloud. In fact, it is evident that K-H growth occurs much earlier (Fig. 3b, *top*).

Model 2 is shown in the bottom panel of Figure 3. This model has the density distribution described in equation (1), with an inner radius $r_i = 0.6 a_0$. The evolution of this model is markedly different from that of model 1 (Fig. 3). The $\chi = 10$ listed in Table 2 is what the density would be at the center of
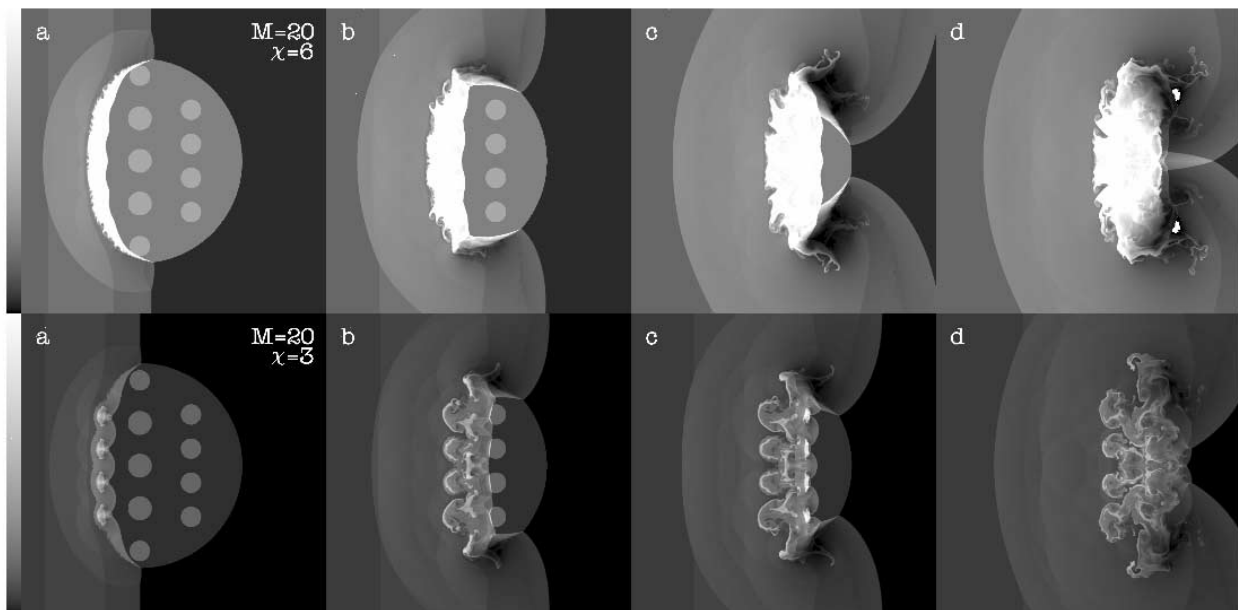

Fig. 4.—Density plots of models 3 (*top*) and 4 (*bottom*). Model 3 is shown at $(1.8, 2.9, 4.0, \text{and } 4.7) \times 10^{-2}$. Model 4 is shown at $(1.7, 3.0, 3.3, \text{and } 4.3) \times 10^{-2}$.
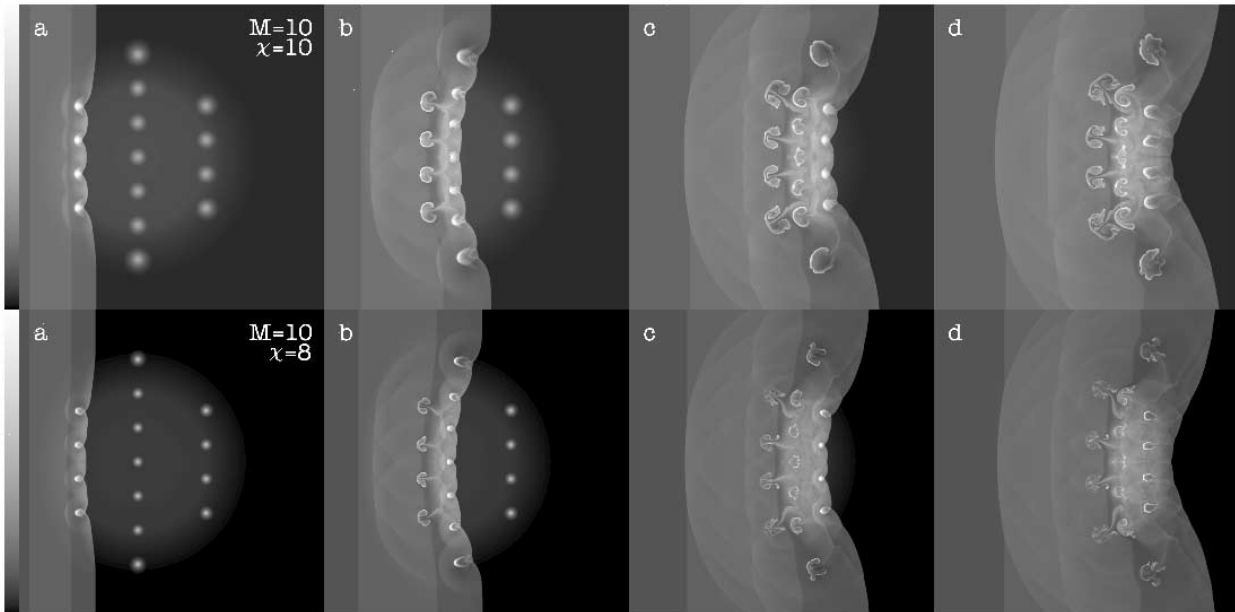
Fig. 5.—Density plots of models 5 (*top*) and 6 (*bottom*). Model 5 is shown at (2.3, 4.6, 6.6, and 7.5)$\times 10^{-2}$. Model 6 is shown at (2.3, 4.3, 6.4, and 7.4)$\times 10^{-2}$.

the Lorentzian. However, since the Lorentzian is truncated at r_i, the effective χ is much lower, by an amount $1/(1 + r_i^2/r_0^2)$. Therefore, the maximum χ in the cloud is ≈ 3, or half the χ of model 1. More important than the lower χ between the two models, model 2 does not show signs of the instability growth seen in model 1. This interesting result lends weight to the notion of a smooth boundary between the ISM and an embedded ISM cloud.

While models 1 and 2 accentuate the differences that arise between a smoothly varying density distribution and that of a sharp-edged cylinder, the remaining models (3–6) simulate how the internal density structure affects the cloud shock. Models 3 and 4 (Fig. 4) are of cylindrical clouds of $\chi = 6$ and 3, respectively. Both clouds contain perturbations with a χ of 10 above the cloud density (or 30 and 60 times the ambient density). In model 3 ($\chi = 6$), the flow around the cloud is still strongly influenced by the higher cloud density. The inclusion of cloudlets results in the formation of shock structure within the cloud (not seen in model 1). However, in the late time (Fig. 4d), the morphology of the cloud is still similar to the late-time morphology of model 1.

The evolution of model 4, on the other hand, is more strongly influenced by the cloudlets. This is because the density contrast between the cloud and the ambient medium here is only 3, and thus the cloud-shock velocity is not significantly different from the blast wave velocity ($\sqrt{3}$ lower). Instead, the blast wave is more influenced by the high-density cloudlets (relative to the cloud), as seen in Figure 4 (*bottom*). While this model reproduces the observed shock diffraction (cf. Fig. 1), the presence of instability growth along the (albeit low-density) model cloud boundary is not something observed in the observations.

Models 5 and 6 represent our best approximations to this diffuse ISM cloud. Physically, the model distributions represent cool, low-density clouds surrounded by warm, lower density envelopes. Within the clouds, cold dense cloudlets are interspersed here on a regular grid. Cloudlet formation is beyond the scope of this paper but is likely a thermal, rather than gravitational condensation.

Model 5, shown in Figure 5 (*top*), is of a Mach 10 shock overrunning a cloud with a density distribution given by equation (1). The cloudlets have a χ of 10 and a maximum extent of

$a_{\mathrm{cloudlet}} = 0.05$. Furthermore, the inner radius of the cloud core is $0.6a_0$, which results in some of the cloudlets being outside of the cloud core.

As seen in Figure 5, the blast wave shock is hardly slowed by its interaction with the cloud, similar to model 4. However, the high-density cloudlets do significantly alter the cloud-shock structure. Compared to model 2 (Fig. 3), the cloudlets appear to play a significant role in slowing the cloud shock.

Model 6 differs from model 5 in three ways: First, the χ of the cloud is 8, rather than 10; second, the χ of the cloudlets is increased to 15, and third, the radius of the cloudlets is 0.03. Model 6 is shown in Figure 5 (*bottom*). Here one sees that the χ of the cloud is so low that it barely slows the shock. Moreover, and probably more importantly, the spacing of the cloudlets is such that they do not feel the effects of their neighbors (i.e., $\Delta r > 4.2a_{\mathrm{cloudlet}}$ and the diffracted shocks are not significantly curved).

Several features appear in the model simulations that are not observed. Prominent in all the models is the formation of a bow shock behind the cloud. A bow shock is not seen in Figure 1 simply because it is moving back into previously ionized material so that there is no neutral population to excite. In models containing cloud clumps (models 3–6), fingers and mushroom heads are prominent in the postshock flow. Three-dimensional models for shock-cloud interactions show that many of these features are unstable and will not persist in three dimensions due to turbulent effects in the postshock flow (Stone & Norman 1992).

6. DISCUSSION

As seen in Figure 1, the southwest cloud of the Cygnus Loop represents a fairly uncomplicated case for investigating many of the basic phenomena of a shock-cloud interaction. The low density of the cloud implies that the cloud shocks will be largely nonradiative in nature. Compared to other regions of the Cygnus Loop (Levenson & Graham 2001 and references therein), the low-density nature of this small cloud allows us to view internal cloud shocks. Furthermore, while the east-west extent of the cloud is not known, the location of the forward shock not interacting with the cloud suggests that this shock-cloud interaction is

relatively young. Thus, this cloud presents a good test case to model the interaction between a SNR shock and an ISM cloud.

6.1. *Comparisons to Other Shock Models*

There have been several previous studies on shock-cloud interactions. Perhaps the best current model for comparison is that of KMC94. Although there is not a one-to-one comparison between our model 1 and their models due to the differing initial condition, many of their conclusions are observed in model 1, such as the formation of K-H instabilities on the order of t_{cc} (Fig. 3c, *top*), like that found in KMC94.

On the other hand, there have been few published studies concerning the interaction between a shock and a cloud with a smoothly varying density. Our models 2, 5, and 6 suggest that much of the instability growth observed in previous studies is related to the chosen geometry. ISM clouds are often modeled as cylinders or spheres with sharp, well-defined boundaries. Yet the real boundary between the ISM and embedded diffuse clouds is likely to be less distinct. However, models in which the density varies over a certain distance such as that described by a hyperbolic tangent (Poludnenko et al. 2002) can sometimes lead to spurious instability growth like that seen in the sharp-edged cylindrical case.

In regard to the internal cloud density structure (cloudlets), Poludnenko et al. (2002) found that the principal parameter is the spacing between the cloudlets. Their models suggested that there exists a critical separation between cloudlets of $\approx 4.2 a_{cloudlet}$, and not surprisingly, the cloudlet spacing in model 5 is about this value. Furthermore, as pointed out by Poludnenko et al. (2002), a larger $\chi_{cloudlet}$ combined with a larger cloudlet spacing does not result in dynamics that are similar to the case of a lower $\chi_{cloudlet}$ combined with a smaller cloudlet spacing. Instead, as evidenced by model 6, the larger separation, regardless of $\chi_{cloudlet}$, results in what are essentially multiple independent interactions between the cloudlets and the cloud shock.

6.2. *The Southwest Cloud*

While the southwest cloud represents a valuable laboratory for investigating the shock-cloud interaction, as evidenced in Figure 1, it is still highly complex on small scales. Hence, the models presented here only approximate its global properties. Based on Figure 1, the cloud has a radius (north-south direction) of $1'-2'$. At the assumed distance of 550 pc, this corresponds to 0.16–0.33 pc, or $\approx (0.5-1) \times 10^{18}$ cm. In model 5, the fiducial radius of the cloud is 0.35. Using model 5 as our potential model for the southwest cloud, the length scale of the model is thus 1.5×10^{15} cm cell^{-1}.

The density of the ISM in this region is estimated to be $\sim 0.1-0.3$ cm^{-3}. The maximum χ for model 5 is 10, but in reality the density profile is truncated at an inner radius $r_i = 0.21 a_0$. At $r_i = 0.21 a_0$, $\chi \approx 4$ for model 5. This agrees with our lower density estimate of $\chi \approx 4.5$ from ram pressure arguments. Thus, the cloud particle density is $\approx 0.4-1.2$ cm^{-3} with a $\chi = 10$ for the individual clumps in model 5 ($n \approx 1.0-3.0$ cm^{-3}). The lower shock velocities seen in the cloud suggest cloudlet χ-values as high as 17, but the difference between a Gaussian profile with a peak density of 10 and one of 17 is minimal.

Based on the size of the grid cell and the shock velocity, the ambient shock traverses one cell in $\sim 10^8$ s $\simeq 3$ yr. The time difference in the proper motion analysis is about 10 years; that is, the ambient shock has traveled three to five cells. In Figure 5, the top panels show the density at $t = (2.2-7.3) \times 10^{-2}$. The simulation begins at $t = 0$, and the shock first hits the cloud at $t = 0.005$. The radius of the cloud is ≈ 500 cells. Therefore, the ambient shock has been traveling for ~ 2000 yr when it reaches the cloud midpoint.

From the X-ray–derived shock velocity of ~ 300 km s^{-1}, Patnaude et al. (2002) estimated the age of the interaction to be ~ 1200 yr, so the modeled cloud size and the shock velocity appear reasonable. At the current epoch, the forward shock is $1'-2'$ ahead of the cloud shock. From Figure 5, the cloud shock lags behind the blast wave by 10% (Fig. 5b, *bottom*). This corresponds to a physical distance of 1.9×10^{17} cm, or 0.5 at a distance of 550 pc. By Figure 5c (*top*), the blast wave is 20% farther along than the cloud shock. Here the morphology of model 5 closely matches that of the southwest cloud (Fig. 1).

The observed internal cloud structure in the Hα image (Fig. 1) is not unlike the modeled shock-cloud internal structure seen in Figure 5. In general, the cloud shocks seen in the Hα image are $\lesssim 0.5$ tip to tip. This scale is consistent with the approximate size of the internal shocks seen in our model 5 (Fig. 5). The cloud shocks have survived the 10 years between observations. The models, however, show that internal shocks are straightened out over a course of a few hundred time steps (~ 200 yr). However, over the short time we are concerned with here, the shock structure of the cloud shock looks remarkably similar to that of the southwest cloud.

7. CONCLUSIONS

A relatively isolated, low-density ISM cloud situated along the southwest limb of the Cygnus Loop provides a particularly clear view of the early stages of a SNR shock–ISM cloud interaction. The combination of multiepoch observations and high-resolution numerical modeling of this cloud has provided some new insights regarding how shocks overrun ISM clouds. The southwest cloud's isolation and low density has also allowed us to view its internal density structure and make inferences concerning the cloud's initial density distribution.

Our specific findings are as follows:

1. Using multiepoch Hα observations of a small, isolated ISM cloud in the southwest portion of the Cygnus Loop, we measured proper motions of Balmer-dominated shock filaments, which wrap around the cloud, as well as the proper motion of several internal cloud shocks. The Balmer-dominated filaments have transverse velocities of $\sim 200-250$ km s^{-1}, while the shock filaments internal to the cloud have transverse velocities of 65–140 km s^{-1}.

2. The shocked cloud's morphology does not show many of the dynamical instabilities predicted by previous shock-cloud models. This suggests that there is no abrupt boundary or edge for diffuse ISM clouds. A sharp density rise between the cloud and the ISM would lead to steep velocity gradients at the shocked cloud–shocked ISM interface. These steep gradients would in turn lead to the onset of Kelvin-Helmholtz instabilities, which are not observed. This conclusion contrasts with the shock-cloud interaction seen in the southeast of the Cygnus Loop, where the blast wave is thought to be interacting with a large, dense cloud, and instability growth is clearly seen along the cloud-shock boundary.

3. Our model hydrodynamic simulations suggest that ISM clouds are best modeled as a constant or smoothly varying core density embedded in lower density envelope that tapers to the surrounding ISM. Ram pressure equilibrium arguments suggest a cloud-ISM density contrast for this cloud of $\chi = 5-17$, with the lower χ-values corresponding to the diffuse regions of the cloud and the upper limit of 17 corresponding to the dense cloud clumps.

4. A definite spacing of dense, small cloudlets inside the cloud is needed to generate the cloud's internal morphology as seen in the Hα image. As pointed out by Poludnenko et al. (2002), clumps spaced too closely together interact with the shock as if they were one large clump, while those spaced too far apart behave as a set of individual clouds. Our models are consistent with the optimal spacing of $d_{\mathrm{crit}} \approx 4a_{\mathrm{cloudlet}}$ (Poludnenko et al. 2002). The observed internal cloud-shock diffraction caused by these cloudlets is a short-lived phenomenon. As the cloud shock interacts with the cloudlets, the diffracted shocks reorder themselves on a timescale on the order of a few cloudlet crossing times.

REFERENCES

Blair, W. P., Sankrit, R., & Raymond, J. C. 2005, AJ, 129, 2268
Blondin, J. M., & Knerr, J. M. 1992, BAAS, 24, 1227
Colella, P., & Woodward, P. R. 1984, J. Comput. Phys., 154, 174
DeNoyer, L. K. 1975, ApJ, 196, 479
Fesen, R. A., Blair, W. P., & Kirshner, R. P. 1982, ApJ, 262, 171
Fragile, P. C., Anninos, P., Gustafson, K., & Murray, S. D. 2005, ApJ, 619, 327
Fragile, P. C., Murray, S. D., Anninos, P., & van Breugel, W. 2004, ApJ, 604, 74
Kahn, F. D. 1976, A&A, 50, 145
Klein, R. I., McKee, C. F., & Colella, P. 1994, ApJ, 420, 213 (KMC94)
Levenson, N. A., & Graham, J. R. 2001, ApJ, 559, 948
Mac Low, M. M., McKee, C. F., Klein, R. I., Stone, J. M., & Norman, M. L. 1994, ApJ, 433, 757
Mellema, G., Kurk, J. D., & Rottgering, H. J. A. 2002, A&A, 395, L13
Nittmann, J., Falle, S. A. E. G., & Gaskell, P. H. 1982, MNRAS, 201, 833
Parker, R. A. R. 1967, ApJ, 149, 363
Patnaude, D. J., Fesen, R. A., Raymond, J. C., Levenson, N. A., Graham, J. R., & Wallace, D. J. 2002, AJ, 124, 2118
Poludnenko, A. Y., Frank, A., & Blackman, E. G. 2002, ApJ, 576, 832
Stevens, I. R., Blondin, J. M., & Pollock, A. M. T. 1992, ApJ, 386, 265
Stone, J. M., & Norman, M. L. 1992, ApJ, 390, L17
Thorstensen, J. R., Fesen, R. A., & van den Bergh, S. 2001, AJ, 122, 297
Tonry, J., & Davis, M. 1979, AJ, 84, 1511
Woodward, P. R. 1976, ApJ, 207, 484